

## Networks of micronized fat crystals grown under static conditions

Nikolaeva, T.; den Adel, R.; Velichko, Evgenii; Bouwman, Wim; Hermida-Merino, D.; van As, H.; Voda, A.; van Duynhoven, J

**Publication date**

2018

**Document Version**

Final published version

**Published in**

Food & Function: linking the chemistry and physics of food with health and nutrition

**Citation (APA)**

Nikolaeva, T., den Adel, R., Velichko, E., Bouwman, W., Hermida-Merino, D., van As, H., Voda, A., & van Duynhoven, J. (2018). Networks of micronized fat crystals grown under static conditions. *Food & Function: linking the chemistry and physics of food with health and nutrition*, 4, Article 4.

**Important note**

To cite this publication, please use the final published version (if applicable).  
Please check the document version above.

**Copyright**

Other than for strictly personal use, it is not permitted to download, forward or distribute the text or part of it, without the consent of the author(s) and/or copyright holder(s), unless the work is under an open content license such as Creative Commons.

**Takedown policy**

Please contact us and provide details if you believe this document breaches copyrights.  
We will remove access to the work immediately and investigate your claim.

***Green Open Access added to TU Delft Institutional Repository***

***'You share, we take care!' – Taverne project***

**<https://www.openaccess.nl/en/you-share-we-take-care>**

Otherwise as indicated in the copyright section: the publisher is the copyright holder of this work and the author uses the Dutch legislation to make this work public.

Cite this: *Food Funct.*, 2018, 9, 2102

## Networks of micronized fat crystals grown under static conditions†

 T. Nikolaeva,<sup>a,b</sup> R. den Adel,<sup>c</sup> E. Velichko,<sup>d</sup> W. G. Bouwman,<sup>d</sup>  
 D. Hermida-Merino,<sup>e</sup> H. Van As,<sup>a,b</sup> A. Voda,<sup>\*c</sup> and J. van Duynhoven<sup>a,c,b</sup>

Dispersing micronized fat crystals (MFCs) in oil is a novel route to largely decouple fat crystallisation and network formation and thus to simplify the manufacture of fat-continuous food products. MFCs dispersed in oil form a weak-interaction network organized by crystal aggregates in a continuous net of crystalline nanoplatelets. The rough surface of MFC nanoplatelets hampers stacking into one-dimensional aggregates, which explains the high mass fractal dimensions of the networks formed in MFC dispersions. Applying shear does not have a significant effect on the fractal dimensions of MFC networks, and MFC aggregates in the range of 5–10 μm remain intact. However, shear leads to a significant loss of storage modulus and yield stress over a time frame of an hour. This can be attributed to irreversible disruption of the continuous net of nanoplatelets. Rheo-SAXS revealed that shear releases nanoplatelets from the continuous net, which subsequently align in the shear field and undergo rapid recrystallisation. The release of thin and metastable nanoplatelets from the weak-link network bears relevance for simplified and more effective manufacturing of emulsified food products by effectively decoupling crystallisation, network formation and emulsification.

Received 23rd January 2018,  
Accepted 13th March 2018

DOI: 10.1039/c8fo00148k

rsc.li/food-function

## 1 Introduction

The shelf-life stability and sensorial quality of fat-based products are for a major part determined by the structure of fat crystal networks.<sup>1,2</sup> These typically adopt a multi-length scale hierarchical organization, which can be manipulated by chemical composition<sup>3–5</sup> and processing routes based on melting and cooling steps.<sup>6,7</sup> During the cooling of a fat melt, lamellar stacks of triacylglycerol (TAG) bilayers grow into crystalline nanoplatelets.<sup>8</sup> They can aggregate to larger structures that are plate-like, needle-like or spherulitic.<sup>9,10</sup> These aggregates form a fractal network, with weak-link interactions between them.<sup>11</sup> The viscoelastic and yield stress properties<sup>7,12,13</sup> of networks formed from the melt strongly depend on the processing conditions during cooling, like

temperature and shear.<sup>14–16</sup> These determine an intricate interplay between formation of fat crystals and their aggregation into larger structures.<sup>17,18</sup> The strong coupling of these two structure formation steps is adding significant complexity to the industrial manufacturing of fat-based food products. This is particularly the case for the industrial manufacturing of fat-continuous food emulsions, where fat crystallisation and network formation occur concomitantly with emulsification.<sup>19,20</sup> For the manufacturing of products with low levels of saturated (solid) fat, current industrial processing routes have reached their processing and formulation limits.<sup>21</sup>

A novel route to largely decouple fat crystallisation and network formation is to disperse pre-crystallized fat nanoplatelets in oil.<sup>22</sup> Such pre-crystallized fat nanoplatelets can be produced by supercritical melt micronisation (ScMM): saturating a molten fat blend with supercritical CO<sub>2</sub>, which is subsequently expanded through a nozzle. The resulting fine powder of rapidly micronized fat crystal (MFC) nanoplatelets can be readily dispersed in oil. By this process, fat crystallisation and network formation can be largely decoupled, which offers opportunities for simplified and flexible manufacturing of fat-continuous food products.<sup>22</sup> However, no detailed investigation on the obtained MFC networks has appeared so far.

In this study we investigated dispersions of micronized fat crystals (MFCs) in oil that were allowed two weeks of network formation. We hypothesized that within these dispersions diffusion- or reaction-limited aggregation of MFCs would form

<sup>a</sup>Laboratory of Biophysics, Wageningen University, Stippeneng 4, 6708WE Wageningen, The Netherlands

<sup>b</sup>MAGNETic resonance research FacilitY (MAGNEFY), Stippeneng 4, 6708WE Wageningen, The Netherlands

<sup>c</sup>Unilever R&D, Olivier van Noortlaan 120, 3133 AT Vlaardingen, The Netherlands. E-mail: adrian.voda@unilever.com

<sup>d</sup>Faculty of Applied Sciences, Delft University of Technology, Mekelweg 15, 2629 JB Delft, The Netherlands

<sup>e</sup>DUBBLE CRG/ESRF, Netherlands Organisation for Scientific Research (NWO), c/o ESRF BP 220, F38043 Grenoble Cedex, France

†Electronic supplementary information (ESI) available. See DOI: 10.1039/c8fo00148k

fractal MFC aggregates which interact *via* weak links. A suite of measurement techniques was used to investigate the multi-scale structure of these networks and their viscoelastic and yield stress properties. At the nanoscale, Wide and Small Angle X-ray Scattering (WAXS, SAXS) were used for the assessment of fat crystal polymorphs and the thickness of the nanoplatelets. Their possible arrangement in stacked aggregates (TAGwoods)<sup>23,24</sup> was studied by means of Ultra Small Angle X-ray Scattering (USAXS). Confocal Raman imaging was deployed to obtain a micron scale view of the fat crystal networks. We used bulk rheology and Magnetic Resonance Imaging (rheo-MRI) to assess viscoelastic and yield stress properties. The macroscopic mechanical properties were modelled using the fractal theory of weak-link networks.<sup>7,11</sup> The fractal nature of the network was assessed by USAXS, confocal Raman imaging and bulk rheology. *In situ* rheo-SAXS experiments were conducted to assess shear-induced sub-micron mesoscale structural rearrangements of MFC dispersions.

## 2 Materials and methods

### 2.1 Materials

Micronized fat crystals (MFCs) were obtained by spraying fat blends dissolved in supercritical CO<sub>2</sub>.<sup>22</sup> The TAG composition of the studied MFCs is presented in Tables SI 1 and SI 2 in the ESI.† The MFCs were dispersed in sunflower oil (SF) by intense mixing under vacuum at a temperature of about 20 °C. The concentration of MFC varied from 5% to 25% (weight). Melt-cool (MC) dispersions were prepared by melting MFC dispersions at 80 °C to erase crystal memory and subsequent cooling to 20 °C at a rate of 0.1 deg min<sup>-1</sup> to induce fat crystallization. The MFC and MC dispersions were stored at 20 °C for two weeks to form a stable network.

### 2.2 Bulk rheology

Rheological measurements were performed with an Anton Paar (MCR302 SN81236695) rheometer using a cone-plate (CP) geometry (cone angle of 3.992°, cone diameter of 49.971 mm). An oscillatory strain program was used to determine the boundaries of the linear viscoelastic region (LVR) from which apparent values of storage modulus  $G'$  were obtained.<sup>20</sup> The rheometer was run through an oscillatory strain program with applied strain ranging from 0.0001 to 100% at a frequency of 1 Hz and at 20 °C. The weak-link theory<sup>25</sup> provides the relationship between the storage modulus  $G'$  of a volume-filling network and the volume fraction of particles.<sup>7,13,25</sup>

$$G' = \lambda \Phi^{\frac{1}{1-D}}$$

where  $G'$  is the shear storage modulus,  $\lambda$  is a constant,  $\Phi$  is the volume fraction and  $D$  is the fractal dimension. The volume fraction of fat crystalline nanoplatelets in the dispersions was assumed to be proportional to the mass concentration,  $c$ . Fractal dimension values of fat crystal dispersions were obtained from the slopes of  $\log G'$  versus  $\log c$ .<sup>20,25</sup>

Two rheological approaches were used to measure yield stress properties of the material. In the first approach the yield stress was defined as the stress value at the limit of linearity of a small deformation mechanical test.<sup>26</sup> In the second one, we determined yield stress values *via* bifurcation measurements:<sup>27,28</sup> a fixed stress was applied and the rate of strain was then measured as a function of time. In each experiment a fresh sample was used. To every sample, we applied a required constant shear rate for 60 s before the oscillatory strain and bifurcation programs. Shear rates varied from 0.1 to 140 s<sup>-1</sup>. The same procedure of applying shear as a pre-shear step was used for the characterization of MFC and MC dispersions by Raman-imaging, WAXS, SAXS and USAXS methods.

### 2.3 Rheo-MRI

Rheo-MRI velocity profiles were obtained using a Bruker Avance III spectrometer at 7.0 T magnetic field strength (resonance frequency 300 MHz for <sup>1</sup>H) in combination with a Bruker rheo-MRI accessory. As a shear cell, the Couette geometry was chosen with serrated walls, and inner and outer cylinder diameters of 17 and 22 mm, respectively, and hence a gap size of 2.5 mm. The inner cylinder rotation speed ranged from 0.25 to 62.38 s<sup>-1</sup>. We measured 1D velocity profiles in 1 mm slice thickness by the Spin Echo (SE) sequence<sup>29</sup> (repetition time  $T_R = 1.5$  s, echo time  $T_E = 17$  ms,  $\Delta = 13.1$  ms,  $\delta = 1$  ms). Local velocities were measured with a field of view of 25 mm and a spatial resolution of 48.8 μm. The time needed to obtain a single velocity profile within the gap was of the order of 3 s. The number of scans (NS) = 64 was chosen to improve the signal-to-noise ratio. The temperature in the Couette geometry was controlled at 20 °C. The stability of the NMR signal indicates that no significant temperature variation occurred during the experiments.

We constructed constitutive relations  $\sigma(\dot{\gamma})$  by combining local stress  $\sigma(r, \omega)$  and local shear rate  $\dot{\gamma}(r, \omega)$ ,<sup>30,31</sup> which were collected at various positions  $r$  within the gap and various angular velocities  $\omega$ . Rheo-MRI velocity data  $v$  gave the magnitude of the local shear rate  $\dot{\gamma}(r, \omega)$ :<sup>32</sup>

$$\dot{\gamma}(r) = r \frac{\partial(v/r)}{\partial r}.$$

The local stress  $\sigma(r, \omega)$  was obtained by performing applied torque  $T$  measurements for each angular velocity. We used a copy of the rheo-MRI Couette cell and a conventional rheometer Modular Compact Rheometer 301 (MCR301 SN80480600, Anton Paar). From torque data the shear stress was estimated<sup>32</sup> as

$$\sigma(r) = \frac{T}{2\pi r^2 H}$$

( $\sigma(r)$  is the local stress as a function of the position,  $T$  is a torque,  $r$  is the position within the gap and  $H$  is the fluid height in the gap), which is valid for a homogeneously distributed material along the vertical direction within the Couette

geometry. The local flow curve was constructed by plotting both  $\sigma(r, \omega)$  and  $\dot{\gamma}(r, \omega)$  in a single  $\sigma(\dot{\gamma})$  plot.

## 2.4 Raman imaging

Full details of the experimental procedures can be found elsewhere.<sup>33,34</sup> In short, experiments were performed on a WITec confocal Raman (Alpha 300R+) microscope equipped with a Zeiss upright microscope with a 532 nm laser at 25.0 mW. The sample was placed on a 19 °C water-cooled plate. The laser was used with a 100×/1.4 NA oil objective. The Raman spectrometer was coupled to a cooled (−60 °C) EMCCD detector. The obtained Raman spectra were in the range of 100–3800  $\text{cm}^{-1}$ . An integration time of 0.01 s was used for imaging a  $200 \times 200$  or  $50 \times 50 \mu\text{m} \times \mu\text{m}$  area with a resolution of 0.23  $\mu\text{m}$ . The raw data were subjected to corrections and multivariate curve resolution (MCR) performed in MATLAB (The MathWorks Inc.) in order to obtain maps of solid fat content.

Fractal dimensions  $D$  were determined by the box-counting method, which assessed fractality with better precision compared to other approaches.<sup>33</sup> An image is overlaid with boxes of decreasing size, determining for each box size how many boxes contain (part of) a self-similar object. The relationship between the number of filled boxes ( $N_b$ ) and the length of the boxes ( $l_b$ ) provides the fractal dimension  $D$ :

$$D = \frac{\Delta \log N_b}{\Delta \log l_b} - 1$$

Fractal dimensions were calculated using MATLAB (The MathWorks Inc.).<sup>33</sup>

## 2.5 WAXS and SAXS

Wide and Small Angle X-ray diffraction (WAXS and SAXS) analyses were performed on a Bruker D8-Discover diffractometer in a  $\theta/\theta$  configuration. The sample-to-detector distance was 32.5 cm. For both SAXS and WAXS measurements a modified Linkam stage was used to adjust temperature. In the WAXS configuration, the type of crystal polymorph of the fat blend was identified. The angle of the incident X-ray beam and the angle between the detector and the sample were 10°, allowing collection of WAXS data in the range of  $7^\circ < 2\theta < 55^\circ$ . In the SAXS mode, the long spacings (thickness of the repeating TAG bi-layers) of the fat crystallites were measured. The average crystal thickness (ACT) was determined by the Scherrer line shape analysis of the first order diffraction peak:<sup>9</sup>

$$d = \frac{K\lambda}{\text{FWHM} \cos \theta}$$

where  $\theta$  and  $\lambda$  are the Bragg angle and the X-ray wavelength, respectively. FWHM is the line width at half of the maximum peak height in radians corrected for instrumental broadening and was calculated using the EVA software from Bruker AXS. The instrumental line broadening is  $2\theta = 0.08^\circ$ , which was determined using the FWHM of the 111 Si reflection of NIST standard reference material 640.  $K$  and  $\lambda$  are 0.9 and 0.15418 nm, respectively. The Scherrer equation indicates an inverse relationship between crystallite thickness and peak

width: the broader the peak, the smaller the crystallites. The crystal thickness distribution (CTD) was determined using the Bertaut–Warren–Averbach (BWA)<sup>35</sup> analysis of the same, first order, diffraction peak.

## 2.6 Rheo-SAXS

The Rheo-SAXS measurements were carried out at the BM26 beamline at the European Synchrotron Radiation Source, Grenoble, France<sup>36–39</sup> A home-built horizontal Couette shear-cell (Fig. 1) allowed the X-ray beam to be directed along the vorticity direction of the flow at different positions across the gap between the inner and outer cylinders. A gap of 1 mm with 38 mm outer radius was used. A rotation speed was applied to the inner cylinder of the Rheo-SAXS cell. MFC dispersions were measured under constant shear for 10 minutes, after which another shear rate was imposed to the same sample. Shear rates applied to the same sample were 0, 1, 5, 35, 70, 100, 140, 1, and 0  $\text{s}^{-1}$ . The beam cross-section at the sample position was about 120  $\mu\text{m}$ , which allowed us to measure five different positions across the gap without overlap. We used the Pilatus detector with a resolution of  $981 \times 1043$  pixels and a pixel size of  $172 \times 172$  microns square positioned at a distance of 1400 mm away from sample for the SAXS measurements with a wavelength of  $\lambda = 1.033 \text{ \AA}$ . The experimental setup allowed us to probe length scales of the order of 4–210 nm. Standard corrections for sample absorption and background subtraction were applied. The data were normalized to the intensity of the incident beam to correct for primary beam intensity fluctuations and were corrected for absorption and background scattering. AgBe has been used as a calibration standard.

To investigate the orientation of fat crystalline nanoplatelets, which have a platelet morphology, two-dimensional (2D) SAXS patterns were collected.<sup>40–42</sup> The orientation distribution was quantified using the integration of the low  $q$  region as a function of the azimuthal angle ( $\chi$ ). The data were fitted using a Gaussian function and the full width at half maximum,  $\Delta\chi$ ,

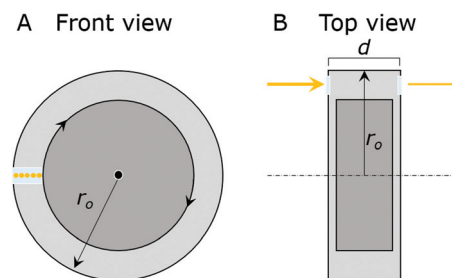


**Fig. 1** A schematic depiction (front (A) and top (B) views) of the home-built horizontal Couette shear-cell used to perform the Rheo-SAXS experiments. The outer radius of the Couette  $r_o$  was 38 mm and a gap size of 1 mm was used. The inner and outer surfaces were serrated. The rotation axis is shown by dot and dash-dot lines on the front and top views, respectively. The beam cross-section was about 120  $\mu\text{m}$  at the sample position. The thickness of the sample  $d$  was 4 mm. The beam and cell windows are indicated by yellow dots and light blue rectangles, respectively.



of the oriented portion and the preferential orientated azimuthal angle,  $\chi_o$ , were estimated. A smaller  $\Delta\chi$  indicates a higher degree of orientation of the lamellar planes.

## 2.7 USAXS

The USAXS measurements were performed at the ID02 beamline<sup>43,44</sup> at the European Synchrotron Radiation Facility (ESRF), Grenoble, France. This USAXS configuration allows for a 30 m distance, which translates into the possibility to access scatterer sizes up to  $\sim 2.5$   $\mu\text{m}$ . The fractal dimensions were determined from USAXS data by means of the Unified Fit (UF) model.<sup>45</sup> Data processing was conducted in Igor Pro 6.37 using the Irena SAS 2.57 package. The USAXS signal of an oil sample was subtracted from the data before data modelling. The Unified Fit model provided two parameters for each structural level  $i$ : the Porod slope,  $P_i$ , and the radius of gyration,  $R_{gi}$ .

$$I_i(q) = \frac{B_i}{q^{P_i}} e^{\left(\frac{-q^2 R_{gi}^2}{3}\right)} \left[ \text{erf}\left(\frac{-q R_{gi}}{\sqrt{6}}\right) \right]^{3P_i}$$

where  $B_i$  is the Porod scale factor that contains specific surface area information.<sup>45,46</sup> The Porod slope,  $P$ , provides information about the crystal surface and morphology and equals the fractal dimension if the system is known to be fractal.<sup>18,47,48</sup> For  $P$  smaller than 3 the fractal dimension equals  $P$  and relates to a mass fractal. Otherwise, the fractal dimension can be calculated as  $6 - P$  and it indicates a surface fractal. The Guinier–Porod (GP) model based on known  $P$  and  $R_g$  was used to estimate the shape of scatterers from the parameter  $s$ :<sup>45–47</sup>  $s = 0$  indicates a spherically symmetric structure,  $s = 1$  a long cylinder indicating the presence of TAGwoods, and  $s = 2$  a thin 2D structure:

$$I(q) = \frac{G}{q^s} \exp\left(\frac{-q^2 R_g^2}{3 - s}\right)$$

where  $G$  is the Guinier factor.

## 3 Results and discussion

### 3.1 Nanoscale and mesoscale characterization

WAXS diffractograms showed that fat nanoplatelets in MFC dispersions occur in the  $\beta$  polymorph (Fig. SI 1 in the ESI†).

This is in line with the  $\beta$  polymorph observed in dispersions prepared by melting-cooling, hereafter referred to as MC dispersions. We note that in the MFC powder the fat nanoplatelets were in the  $\beta'$  polymorph, but upon dispersion in sunflower oil and storage under ambient conditions ( $\sim 20$  °C) rapid (hours) conversion to the  $\beta$  form occurred. The predominance of the  $\beta$  polymorph in aged MC and MFC dispersions relates to high levels of saturated triglycerides that have a preference to crystallize in this stable form. The average fat crystal thickness (ACT) in MFC and MC dispersions was obtained by modelling the first order diffraction line recorded in SAXS by means of the Scherrer equation 9 (Table 1). On increasing the MFC concentration, the ACT decreases from 66 to 52 nm. Comparison of the ACT in MC vs. MFC dispersions revealed thinner crystalline nanoplatelets in the latter, which can be attributed to more rapid crystallisation during micronisation.

We used the Guinier–Porod (GP) and the Unified Fit (UF) models to retrieve mesoscale structural information<sup>23,46–48</sup> from the USAXS curves (Fig. SI 2 in the ESI†). In the  $q$  range  $0.02 < q < 0.1$   $\text{nm}^{-1}$ , which was representative for the nano- and mesoscale of fat crystal networks,<sup>47,48</sup> we observed a Porod slope  $P_1 = 3.2$  for 20% MFC dispersions. This indicated the presence of nanoplatelets with a rough surface (surface fractal dimension  $D_s = 2.8 \pm 0.1$ ,  $R_{g1} = 62 \pm 3$  nm). For the 20% MC dispersions the Porod slope was  $P_1 = 3.6$  (surface fractal dimension  $D_s = 2.4 \pm 0.1$ ,  $R_{g1} = 114 \pm 4$  nm), which indicated the presence of nanoplatelets with a less rough surface.

The next structural level observed by USAXS was in the range of  $0.002 < q < 0.02$   $\text{nm}^{-1}$ , which covers crystal aggregates up to 2  $\mu\text{m}$ . At this structural level the GP model was used to estimate the shape of scatterers from the parameter  $s$ .<sup>45–47</sup> Here  $s = 0$  indicates a spherically symmetric structure,  $s = 1$  a long cylinder or a fibrillar structure indicating the presence of well-stacked nanoplatelets, and  $s = 2$  a thin 2D structure. We obtained values of  $s = 2.4 \pm 0.1$  and  $s = 1.8 \pm 0.1$  for MFC and MC dispersions, respectively. The low value of  $s$  for MC dispersions indicated the presence of TAGwoods, which were likely to form due to the significant amount of tripalmitin (PPP) (Table SI 1 in the ESI†). Under slow crystallization conditions PPP can form pure and smooth crystals, which are prone to stack into TAGwoods.<sup>9,24,47,48</sup> The higher  $s$  values for MFC dispersions can be explained by rapid crystallisation during

**Table 1** Overview of structural parameters derived from 20% MFC and MC dispersions by means of WAXS, SAXS and USAXS using the Scherrer equation (SE) to the first order diffraction line, the Unified Fit (UF) and Guinier–Porod (GP) models. The UF model covered two structural levels and provided the Porod slope,  $P$ , and the radius of gyration,  $R_g$  for each of them. For fractal systems the Porod slope,  $P$ , equals a mass fractal dimension ( $D_m$ ) if  $P$  is smaller than 3.<sup>18,47,48</sup> Otherwise, the fractal dimension can be calculated as  $6 - P$  indicating a surface fractal ( $D_s$ )

		$q$ range [ $\text{nm}^{-1}$ ]	MFC dispersions	MC dispersions
WAXS			Polymorph	$\beta$
SAXS	SE*		ACT [nm]	$82 \pm 0.3$
USAXS	UF*	$0.02 < q < 0.1$ (level 1, $i = 1$ )	$P_1$	$3.6 \pm 0.1$
			$D_s$	$2.4 \pm 0.1$
			$R_{g1}$ [nm]	$114 \pm 4$
		$0.002 < q < 0.02$ (level 2, $i = 2$ )	$P_2$ ( $D_m$ )	$1.8 \pm 0.1$
	GP*	$0.002 < q < 0.02$	$s$	$1.8 \pm 0.1$

supercritical melt micronisation (ScMM). This process induces growth of mixed MFC nanoplatelets with rough surfaces, which are less prone to stacking interactions and formation of TAGwoods.

### 3.2 Micron-scale characterisation

We investigated the microstructure of MCF and MC dispersions by non-invasive confocal Raman imaging. Micron-scale compositional maps of solid fat<sup>33,34</sup> are shown in Fig. 2. The MC dispersions were made up of aggregates of 15–20 micrometres, while in MFC dispersions, nanoplatelets were clustered into aggregates with sizes in the range of 5–10 micrometres. These MFC aggregates appear to be randomly distributed in space. The compositional maps<sup>33,34</sup> showed that the solid fat content (SFC) of the aggregates was of the order of 30–33%, indicating a highly porous structure. The continuous oil phase showed the presence of 13–18% SFC, although no aggregates could be discerned there. The presence of solid fat in the continuous phase suggested the existence of a weak-link network between the randomly distributed aggregates in the MFC dispersion.

### 3.3 Fractal network characterisation

Mass fractal dimensions ( $D_m$ ) were determined by USAXS and small deformation rheology. From USAXS measurements we estimated  $D_m$  based on the Porod slope in the  $0.002 < q < 0.02 \text{ nm}^{-1}$  range using the UF model (Table 1). For MFC dispersions a value of  $D_m = 2.4 \pm 0.1$  was obtained, which was independent of the MFC concentration (data not shown). The mass fractal dimension of MFC networks is significantly higher than that observed for MC dispersions where we obtained  $D_m = 1.8 \pm 0.1$  (Table 1), which is in line with values reported in the literature for dispersions prepared from the melt.<sup>46,48</sup> We also obtained mass fractal dimensions by modelling the dependency of the storage modulus on MFC level by means of the weak-link formalism.<sup>13,25</sup> Thus, for MFC dispersions  $D_m = 2.7 \pm 0.14$  was determined. Differences between the mass fractal dimensions  $D_m$  obtained by USAXS and rheology have been observed previously.<sup>18</sup> These differences have been

attributed to differences in modelling approaches and underlying assumptions considered to determine the fractal dimension based on different experimental techniques. These pertain to different length scales observed by USAXS and rheology and the assumption of self-similarity of fat crystal networks and the weak-link scaling theory<sup>25</sup> to describe small deformations in rheology.

The lower fractal dimension for MC dispersions indicates that cluster–cluster aggregation mechanisms such as Reaction or Diffusion-Limited Cluster–Cluster Aggregation (RLCCA or DLCCA) are at play.<sup>9,18,49–51</sup> Such mechanisms are in line with the previously observed stacking of nanoplatelets in TAGwoods.<sup>24</sup> The aggregation of TAGwoods will then form networks with a low fractal dimension ( $D_m < 2$ ).<sup>47,48</sup> The nanoplatelets that are dispersed in MFC dispersions have rough surfaces, which will impede stacking interactions between them. In this case, Reaction-Limited particle–cluster and Cluster–Cluster Aggregation (RLA and RLCCA) are likely aggregation mechanisms because many collisions between particles or pairs of fat clusters are required before forming a larger aggregate. This will lead to mass fractals of the order of 2.5–3, which is close to the observed values by USAXS ( $D_m = 2.4 \pm 0.1$ ) and rheology ( $D_m = 2.7 \pm 0.14$ ).

### 3.4 Impact of shear on storage modulus and yield stress

To understand the effect of shear on the MFC network structure we assessed its impact on elastic and yield stress properties. Rheology measurements by oscillation sweep experiments were conducted on aged MFC dispersions in a cone-plate configuration. These dispersions were subjected to pre-shear treatment, with shear rates ranging from 0.1 to  $140 \text{ s}^{-1}$ . The storage modulus  $G'$  was obtained in the linear viscoelastic region (LVR) as a function of the pre-shear rate (Fig. 3A).

We observed that the pre-shear treatment leads to a significant decrease of the storage modulus  $G'$  for all the studied MFC concentrations (5, 10, 15 and 20 wt%). We also measured the yield stress as a stress value at the limit of linearity of shear storage modulus  $G'$ <sup>26</sup> (Fig. 3B). The yield stress of the MFC dispersions significantly decreased after pre-shear. We also performed velocity bifurcation measurements to investigate the yield stress properties of MFC dispersions after applying different shear rates<sup>27,52</sup> (Fig. SI 3 in ESI†) and a similar result was obtained.

We used rheo-MRI velocimetry to provide a non-invasive view of the shear strength and time-dependence of the loss of yield stress properties in MFC dispersions. For this purpose, we monitored 10% MFC dispersions in a Couette geometry with a 1 mm gap for an hour at fixed shear rates, which were varied from 0.25 to  $62.38 \text{ s}^{-1}$ . Velocity profiles were collected as a function of position in a 1 mm thick slice of the material. MRI-velocity profiles as a function of shear rate can be found in the ESI (Fig. SI4†). Fig. 4A shows the changes of velocity over the gap at an applied shear rate of  $6.24 \text{ s}^{-1}$  as a function of time. Over time, all the obtained velocity profiles showed a flowing and a static region. We attributed this shear banding behaviour to a combination of heterogeneity of stress over the gap and the

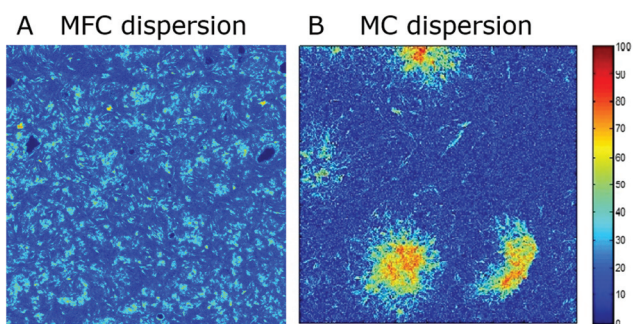


**Fig. 2** The spatial distribution of solid fat of 20% dispersions of (A) MFC and (B) MC in oil as obtained by MCR on confocal Raman images ( $200 \times 200 \mu\text{m}$ ,  $843 \times 843$  spectra). The bar on the right-side indicates the amount of solid fat in percentage.

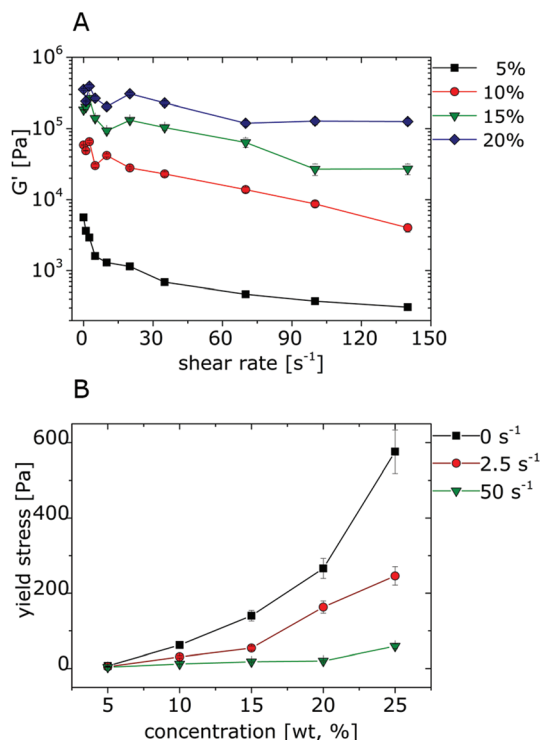


**Fig. 3** (A) Shear storage modulus  $G'$  as function of the pre-shear rate ( $0.1$ – $140\text{ s}^{-1}$ ) for MFC dispersions with solid fat concentrations of 5 ( $\square$ ), 10 ( $\circ$ ), 15 ( $\nabla$ ) and 20 ( $\diamond$ ) %. (B) Effect of pre-shear ( $0$ ,  $2.5$ , and  $50\text{ s}^{-1}$ ) on yield stress as a function of MFC concentration (solids fraction). A constant shear rate was applied to the sample for 60 seconds before the measurement of shear storage modulus  $G'$  and yield stress. The lines connecting the data points are given for eye guidance.

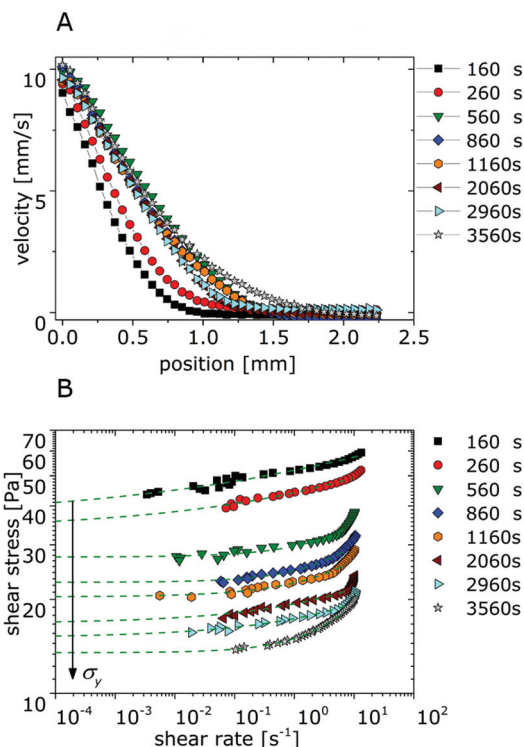


**Fig. 4** MRI-velocity profiles (A) and local flow curves (B) for a dispersion of 10% MFC in oil under a shear rate of  $6.24\text{ s}^{-1}$  as a function of time. For every experiment, a new sample was taken and monitored for 1 hour at a fixed applied shear rate. Rheo-MRI velocity profiles (coexistence of a flowing and a static region) and local flow curves demonstrate yield stress behaviour of MFC dispersions over 1 hour. Dotted green lines in (B) are fits of the Herschel–Bulkley model to the local flow curves. The arrow schematically indicates the loss of yield stress of the MFC network.

presence of a yield stress fluid. The yield stress can be estimated from the constitutive relation  $\sigma(\dot{\gamma})$ , also known as the local flow curve.<sup>53,54</sup> Fig. 4B shows how local flow curves changed over 1 hour under a constant shear of  $6.24\text{ s}^{-1}$ . We used the Herschel–Bulkley model<sup>55,56</sup> to fit the local flow curves and to estimate the apparent yield stress of the MFC dispersion. Structure degradation was apparent as a shift of the local flow curves towards lower stress values. The fits of the Herschel–Bulkley model indicated that this was largely due to a decrease of the yield stress in the flowing band. Note that in the local flow curve only the flowing part of the velocity profile is represented; throughout the measurements the static band slowly decreased in width. A continuous disruption of the crystal network at the applied shear rate of  $6.24\text{ s}^{-1}$  occurred over a time frame of an hour. This continuous disruption was also observed at higher shear rates (data not shown).

The rheology and rheo-MRI experiments demonstrated that shear leads to a significant and continuous disruption of MFC networks at a time scale of an hour. In the next section the underlying microstructural changes are investigated.

### 3.5 Impact of shear on network fractal dimension

To further understand the effect of shear on the MFC network structure we assessed the impact on fractal dimensions.

Monitored by rheology, Raman imaging and USAXS, the changes of the fractal dimensions upon shear are small and within standard experimental error for every applied technique (Fig. 5). The data indicated a weak trend towards an increased fractal dimension upon the application of low shear, suggesting that the distribution of the structural elements became more random. Overall, the data showed that the fractal dimensions  $D$  of the MFC network were not sensitive to mild shear ( $<140\text{ s}^{-1}$ ) and stayed invariant. Average fractal dimensions obtained by the confocal Raman imaging, rheology or USAXS were statistically different, in line with previous observations that these techniques probe fractality at different length scales.<sup>18</sup>

Next, we assessed whether the sizes of MFC aggregates were affected by shear. Raman imaging showed that these MFC aggregates were between  $5$  and  $10\text{ }\mu\text{m}$ , which were invariant to shear. USAXS showed no changes in scattering (Fig. SI 5 in ESI†) in a wide length scale ( $0.005$ – $2.5\text{ }\mu\text{m}$ ). No fat crystal stacks or aggregates with radius of gyration  $R_g$  below  $2.5\text{ }\mu\text{m}$  could be identified. This is either the effect of ageing, in which case the clusters have grown larger, or due to heterogeneous size distribution, such that statistically the scattering



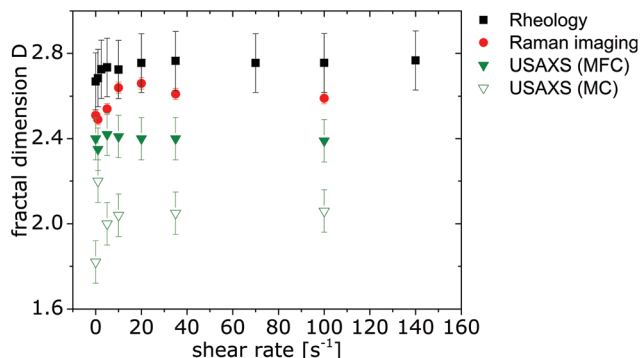


**Fig. 5** Fractal dimensions ( $D$ ) of aged MFC dispersions as a function of pre-shear rates. Black squares represent the  $D$  values obtained by rheology using the colloidal gel fractal theory; red circles and green triangles, respectively, describe  $D$  values obtained by Raman imaging and USAXS for a 10% MFC dispersion. Empty green triangles show the  $D$  values obtained by USAXS for a 10% MC fat crystal dispersion.

function is smeared by a multitude of scatters of different sizes. However, Raman imaging and USAXS data demonstrated that applying shear does not lead to significant destruction of structure in the range of 1–10 micrometres.

### 3.6 Impact of shear on the sub-micron fat crystal network

In order to investigate whether shear has an impact on sub-micron structures we pursued our investigations by Rheo-SAXS. 2D SAXS patterns were collected in the initial unperturbed state and under the application of shear. We did not notice effects of applied shear on the transmission coefficient  $s$  (Fig. SI 7 in ESI<sup>†</sup>), indicating that the effects of melting or dissolution were negligible. The selected 2D patterns shown in Fig. 6 were taken from an oil dispersion containing 20% of MFC under the starting conditions (A) and at shear rates of 5 s<sup>-1</sup> (B) and 70 s<sup>-1</sup> (C). For further discussions we focused on the first order diffraction peak at  $q = 1.5994 \text{ nm}^{-1}$ , which is indicated in Fig. 6.  $q$ -Dependencies of the scattered intensity can be founded in the ESI (Fig. SI 6<sup>†</sup>). The first SAXS pattern for MFC dispersions under the starting static conditions (Fig. 6A) clearly showed an isotropic diffraction peak characteristic of randomly, non-oriented material. Under imposed shear we obtained 2D SAXS patterns that revealed structural an-

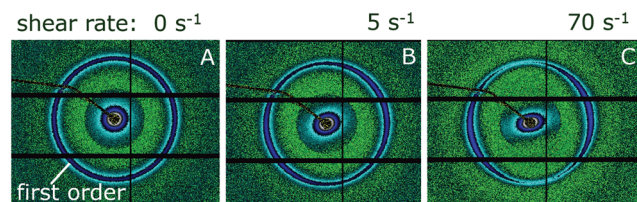


**Fig. 6** Selected 2D SAXS patterns for a 20% MFC dispersion in oil at shear rates of 0 (A), 5 (B) and 70 (C) s<sup>-1</sup>, respectively. The black spot in the center of the image is the beam stop to protect the detector from direct X-ray exposure and the black stripes correspond to the physical gaps of the detector.

isotropy (Fig. 6B and C), indicating that scattering structures were oriented along a preferred direction during the application of shear. The observed alignment under the shear rate was in line with Peclet number estimates<sup>14,40</sup> of  $Pe > 10$  for MFC nanoplatelets with length/widths of 200–400 nm at shear rates in the 1–10<sup>2</sup> s<sup>-1</sup> range. Considering that MFC aggregates up to 2.5  $\mu\text{m}$  were not affected by shear, the scattering structures that align must be MFC platelets that were not part of an aggregate.

We took the radial integral of the 2D patterns at  $q = 1.5994 \text{ nm}^{-1}$  to estimate the amount of oriented crystal nanoplatelets. Fig. 7A shows the integration of 2D SAXS patterns of a 20% MFC dispersion obtained under shear rates in the range between 1 and 140 s<sup>-1</sup>. Here we monitored the number of oriented MFC nanoplatelets as a function of azimuthal angle  $\chi$  extension. Two peaks with a separation of 180° (Fig. 7A) represented the oriented nanoparticles along the flow direction. Under the starting static conditions (0 s<sup>-1</sup>) already some alignment can be observed, likely due to manipulation of the sample into the shear cell. On increasing the shear rate the intensity of anisotropic peaks on  $\chi$  extension increased, which was reflected in a decrease of  $\Delta\chi$  (Fig. 7B). This can be explained by shear-

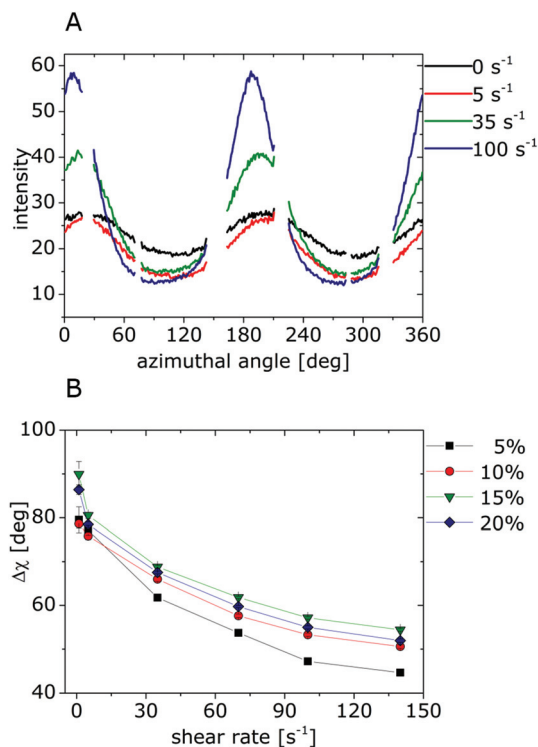


**Fig. 7** (A) Azimuthal angle  $\chi$  extension patterns from radial intensity averaging of 2D SAXS patterns at  $q = 1.5994 \text{ nm}^{-1}$ . The  $\chi$  extension patterns show intensity changes for a 20% MFC dispersion at shear rates of 0, 1, 5, 35, 70, 100, 140, 1, and 0 s<sup>-1</sup>, which were applied for 10 min one after the other. The variation of shear rates was indicated by different colors. The missing points correspond to the physical gaps of the detector. In (B) the full width at half maximum  $\Delta\chi$  is shown as a function of shear rate (0–140 s<sup>-1</sup>) for MFC dispersions with solid fat contents of 5 (□), 10 (○), 15 (▽) and 20% (◇).

induced disruption of the weak MFC network in the continuous phase and subsequent orientation of the released platelets along the shear field. The degree of orientation (alignment) of the MFC nanoplatelets slightly changed at different shear rates (Fig. 7A). Fits of the  $\chi$  extension patterns by a Gaussian function provided estimates of the preferential orientated azimuthal angle  $\chi_0$  (Fig. SI 8 in ESI†). The degree of alignment of MFC nanoplatelets depended on the strength of applied shear and showed the same trend for all the studied concentrations of MFC dispersions. On the variation of shear rate from 1–140  $\text{s}^{-1}$  the degree of alignment changed to approximately  $150^\circ$ . We attribute this small deviation from full alignment of platelets with the flow direction at low shear rates to a small degree of platelet stacking.<sup>57</sup> On increasing the shear rate the MFC nanoplatelets fully aligned to the flow direction, indicating loss of the residual stacking interactions.

### 3.7 Shear-induced recrystallisation in MFC networks

Fig. 8A shows that the ACTs increased for all the studied dispersions when shear was applied (1–140  $\text{s}^{-1}$ ). At the minute

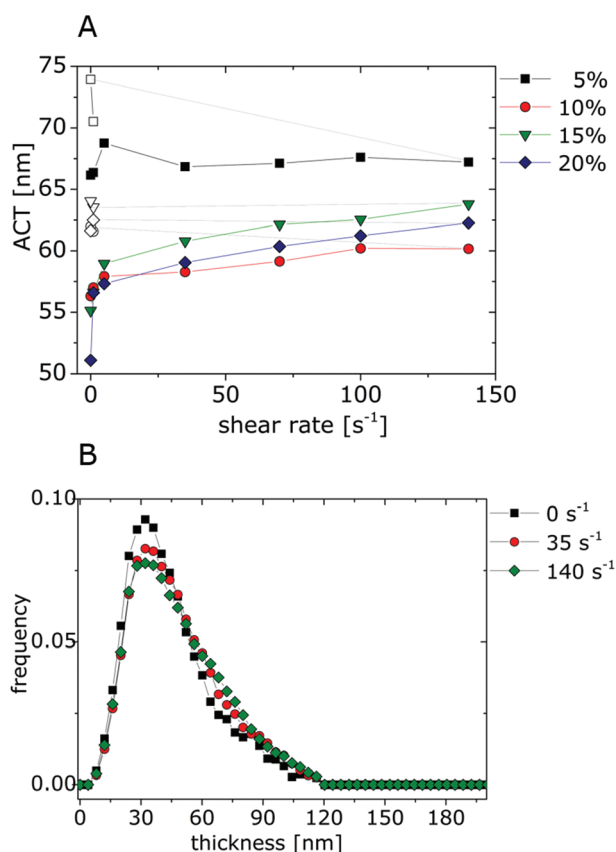


**Fig. 8** (A) Average Crystal Thickness (ACT) as a function of shear rates 0, 1, 5, 35, 70, 100, 140, 1, and 0  $\text{s}^{-1}$ , which were applied to 5% ( $\square$ ), 10% ( $\circ$ ), 15% ( $\nabla$ ) and 20% ( $\diamond$ ) MFC dispersions for 10 minutes one after the other. Empty symbols show the ACT values for the last two steps 1 and 0  $\text{s}^{-1}$  of the shear protocol. (B) Crystal Thickness Distribution (CTD) of fat nanoplatelets obtained after preshear (0, 35 and 140  $\text{s}^{-1}$ ) of a 20% MFC dispersion for 1 minute.

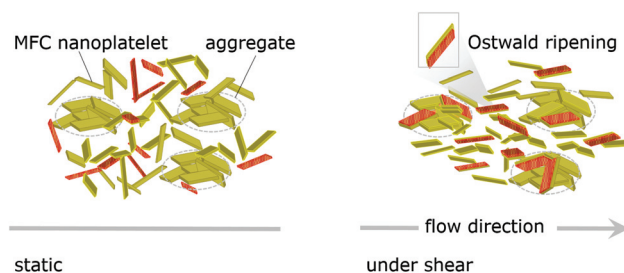


**Fig. 9** Schematic drawing of MFC networks under static and shear conditions. The networks consist of aggregates and a continuous weak-link net of crystalline nanoplatelets. Thin nanoplatelets are indicated in red. Applying shear leads to Ostwald ripening and an alignment of nanoplatelets from the weak-link net along the flow direction. Ostwald ripening is depicted as recrystallisation of thin (red) nanoplatelets onto thicker ones.

time scale of the rheo-SAXS experiment the increase of ACTs occurred immediately. After the application of shear and returning to the static conditions, the ACTs remained the same. To verify whether the ACT values originated from a unimodal distribution, we assessed the impact of shear on the crystal thickness distribution (CTD). Fig. 8B shows CTDs for a 15% MFC dispersion under static conditions and at shear rates of 35 and 140  $\text{s}^{-1}$ . In all cases we observed unimodal distributions and a tendency of the CTD to shift towards larger crystal thicknesses with increasing shear. This is in line with rapid Ostwald ripening, where the thinner MFC nanoplatelets dissolve and recrystallize on the existing nanoplatelets from the weak-link net preferably and likely also on top of the outer nanoplatelets of MFC aggregates (Fig. 9).

In the networks grown under static conditions, the thin platelets are kinetically trapped in a metastable state, until their release by mild shear. This offers opportunities for stabilizing water-droplet interfaces during the manufacturing of fat-continuous food emulsions, and thus more effective use of solid fat crystals. Hence, besides process simplification by decoupling fat crystallization, network formation and emulsification, also lower fat levels may be achieved.

## 4 Conclusions

Under static conditions, MFC dispersions form a weak-link network organized by aggregates connected by a continuous net of dispersed nanoplatelets. During network formation the rough MFC surfaces impede stacking interactions and the formation of TAGwoods. The MFC network fractal dimension ( $D = 2.4$ , USAXS) is higher than that for networks formed from the melt ( $D = 1.8$ – $2.2$ , USAXS), indicating that the particle-cluster mechanism of aggregation is dominant. Rheo-MRI measurements show that under shear yield stress is slowly lost. The application of shear does not affect the size of the MFC aggregates, but does induce the release of nanoplatelets from the weak-link continuous net and subsequent alignment along the flow direction. The network grown under static con-

ditions is metastable; under shear, rapid recrystallisation of the thinner nanoplatelets occurs. The presence of thin platelets in a metastable network grown under static conditions offers opportunities for simplified formulation and processing routes for the manufacturing of low-fat food products.

## Conflicts of interest

J. van Duynhoven, R. den Adel and A. Voda are employed by a company that manufactures and markets fat-based food products.

## Acknowledgements

The authors thank Daan de Kort for advice on the rheo-MRI experiments and Karlijn Theunissen for skilfully performing the rheology measurements. Koen Martens and Patricia Heussen are gratefully acknowledged for measuring the confocal Raman images. The authors thank Kees van Malssen, Jan Wieringa, Jo Janssen, Michiel Meeuse and Peter de Groot from Unilever Discover Vlaardingen for fruitful discussions. The authors thank Wim Bras (NWO) and Gerrit Peters (TUE) for advice on the design of the rheo-SAXS cell. The authors thank the Delft workshop at Delft University of Technology for designing the rheo-SAXS shear cell. The USAXS and Rheo-SAXS experiments were, respectively, performed on beamlines ID02 and BM26 at the European Synchrotron Radiation Facility (ESRF), Grenoble, France. The authors thank T. Narayanan and M. Sztucki for support during experiments on the ID02 beamline at ESRF. This work is part of the research programme SSCANFOODS (project number 13386), which is financed by the Netherlands Organisation for Scientific Research (NWO).

## References

- 1 P. R. R. Ramel, F. Peyronel and A. G. Marangoni, *Food Chem.*, 2016, **203**, 224–230.
- 2 R. Campos, M. Ollivon and A. G. Marangoni, *Cryst. Growth Des.*, 2010, **10**, 205–217.
- 3 A. Bell, M. H. Gordon, W. Jirasubkunakorn and K. W. Smith, *Food Chem.*, 2007, **101**, 799–805.
- 4 M. Zárubová, V. Filip, L. Kšandová, J. Šmidrkal and I. Piska, *J. Food Eng.*, 2010, **99**, 459–464.
- 5 R. W. Hartel, *Annu. Rev. Food Sci. Technol.*, 2013, **4**, 277–292.
- 6 I. Piska, M. Zárubová, T. Loužecký, H. Karami and V. Filip, *J. Food Eng.*, 2006, **77**, 433–438.
- 7 B. A. Macias-Rodriguez and A. A. Marangoni, *Crit. Rev. Food Sci. Nutr.*, 2017, 1–18.
- 8 N. C. Acevedo and A. G. Marangoni, *Cryst. Growth Des.*, 2010, **10**, 3334–3339.
- 9 P. R. Ramel, E. D. Co, N. C. Acevedo and A. G. Marangoni, *Prog. Lipid Res.*, 2016, **64**, 231–242.
- 10 N. C. Acevedo and A. G. Marangoni, *Annu. Rev. Food Sci. Technol.*, 2014, **6**, 1–26.
- 11 A. G. Marangoni, *Fat Crystal Networks*, CRC Press, 2004.
- 12 J. Gonzalez-Gutierrez and M. G. Scanlon, in *Structure-function analysis of edible fats*, ed. A. G. Marangoni, AOCS Press, 2012, vol. 5, pp. 127–172.
- 13 S. Narine and A. Marangoni, *Phys. Rev. E: Stat. Phys., Plasmas, Fluids, Relat. Interdiscip. Top.*, 1999, **59**, 1908–1920.
- 14 F. Maleky, *Curr. Opin. Food Sci.*, 2015, **4**, 56–63.
- 15 D. Dhonsi and A. G. F. Stapley, *J. Food Eng.*, 2006, **77**, 936–942.
- 16 T. Tran and D. Rousseau, *Food Res. Int.*, 2016, **81**, 157–162.
- 17 K. Sato and S. Ueno, *Curr. Opin. Colloid Interface Sci.*, 2011, **16**, 384–390.
- 18 D. A. Pink, F. Peyronel, B. Quinn, P. Singh and A. G. Marangoni, *J. Phys. D: Appl. Phys.*, 2015, **48**, 384003.
- 19 D. Rousseau, *Food Res. Int.*, 2000, **33**, 3–14.
- 20 A. Marangoni and L. Wesdorp, *Structure and Properties of Fat Crystal*, 2013.
- 21 A. Bot and E. Floter, *Application of Edible Oils*, John Wiley & Sons, Chichester, UK, 2nd edn, 2013.
- 22 P. Münüklü and P. J. Jansens, *J. Supercrit. Fluids*, 2007, **40**, 433–442.
- 23 D. A. Pink, B. Quinn, F. Peyronel and A. G. Marangoni, *J. Appl. Phys.*, 2013, **114**, 234901.
- 24 D. A. Pink, B. Townsend, F. Peyronel, E. D. Co and A. G. Marangoni, *Food Funct.*, 2017, 3621–3635.
- 25 W.-H. Shih, W. Shih, S.-I. Kim, J. Liu and I. Aksay, *Phys. Rev. A*, 1990, **42**, 4772–4779.
- 26 A. G. Marangoni and M. A. Rogers, *Appl. Phys. Lett.*, 2003, **82**, 3239–3241.
- 27 D. W. de Kort, S. J. Veen, H. Van As, D. Bonn, K. P. Velikov and J. P. M. van Duynhoven, *Soft Matter*, 2016, **12**, 4739–4744.
- 28 P. Coussot, Q. D. Nguyen, H. T. Huynh and D. Bonn, *J. Rheol.*, 2002, **46**, 573.
- 29 P. T. Callaghan, *Translational Dynamics and Magnetic Resonance: Principles of Pulsed Gradient Spin Echo NMR*, Oxford University Press, Oxford, 2011.
- 30 G. Ovarlez, F. Bertrand and S. Rodts, *J. Rheol.*, 2006, **50**, 1–32.
- 31 P. Coussot, *Rheometry of pastes, suspensions, and granular materials: applications in industry and environment*, Wiley, Hoboken, N.J., 2005.
- 32 R. B. Bird, *Dynamics of polymeric liquids. Vol. 2*, Wiley, New York, Chichester, 1987, vol. 2.
- 33 K. J. A. Martens, G. van Dalen, P. C. M. Heussen, M. A. Voda, T. Nikolaeva and J. P. M. van Duynhoven, *J. Am. Oil Chem. Soc.*, 2018, DOI: 10.1002/aocs.12035.
- 34 G. van Dalen, E. J. J. van Velzen, P. C. M. Heussen, M. Sovago, K. F. van Malssen and J. P. M. van Duynhoven, *J. Raman Spectrosc.*, 2017, 1075–1084.
- 35 V. A. Drits, D. D. Eberl and J. I. Srodoj, *Clays Clay Miner.*, 1998, **46**, 38–50.
- 36 S. Nikitenko, A. M. Beale, A. M. J. Van Der Eerden, S. D. M. Jacques, O. Leynaud, M. G. O'Brien,

- D. Detollenaere, R. Kaptein, B. M. Weckhuysen and W. Bras, *J. Synchrotron Radiat.*, 2008, **15**, 632–640.
- 37 M. Borsboom, W. Bras, I. Cerjak, D. Detollenaere, D. Glastra van Loon, P. Goedtkindt, M. Konijnenburg, P. Lassing, Y. K. Levine, B. Munneke, M. Oversluizen, R. van Tol and E. Vlieg, *J. Synchrotron Radiat.*, 1998, **5**, 518–520.
- 38 W. Bras, I. P. Dolbnya, D. Detollenaere, R. van Tol, M. Malfois, G. N. Greaves, A. J. Ryan and E. Heeley, *J. Appl. Crystallogr.*, 2003, **36**, 791–794.
- 39 G. Portale, D. Cavallo, G. C. Alfonso, D. Hermida-Merino, M. Van Drongelen, L. Balzano, G. W. M. Peters, J. G. P. Goossens and W. Bras, *J. Appl. Crystallogr.*, 2013, **46**, 1681–1689.
- 40 G. Mazzanti, S. E. Guthrie, E. B. Sirota, A. G. Marangoni and S. H. J. Idziak, *Cryst. Growth Des.*, 2003, **3**, 721–725.
- 41 G. Mazzanti, A. G. Marangoni and S. H. J. Idziak, *Food Res. Int.*, 2009, **42**, 682–694.
- 42 K. Sato, L. Bayés-García, T. Calvet, M. À. Cuevas-Diarte and S. Ueno, *Eur. J. Lipid Sci. Technol.*, 2013, **115**, 1224–1238.
- 43 M. Sztucki, J. Gorini, J. P. Vassalli, L. Goirand, P. Van Vaerenbergh and T. Narayanan, *J. Synchrotron Radiat.*, 2008, **15**, 341–349.
- 44 M. Sztucki and T. Narayanan, *J. Appl. Crystallogr.*, 2007, **40**, 459–462.
- 45 F. Peyronel, J. Ilavsky, G. Mazzanti, A. G. Marangoni and D. A. Pink, *J. Appl. Phys.*, 2013, **114**, 234902.
- 46 F. Peyronel, B. Quinn, A. G. Marangoni and D. A. Pink, *J. Phys.: Condens. Matter*, 2014, **26**, 464110.
- 47 F. Peyronel, D. A. Pink and A. G. Marangoni, *Curr. Opin. Colloid Interface Sci.*, 2014, **19**, 459–470.
- 48 F. Peyronel, J. Ilavsky, D. A. Pink and A. G. Marangoni, *Lipid Technol.*, 2014, **26**, 223–226.
- 49 V. I. Roldughin, *Russ. Chem. Rev.*, 2003, **72**, 823.
- 50 P. Meakin, *J. Sol-Gel Sci. Technol.*, 1999, **15**, 97–117.
- 51 P. Meakin and F. Family, *Phys. Rev. A*, 1988, **38**, 2110–2123.
- 52 P. Coussot, Q. D. Nguyen, H. T. Huynh and D. Bonn, *Phys. Rev. Lett.*, 2002, **88**, 175501.
- 53 G. Ovarlez, F. Mahaut, S. Deboeuf, N. Lenoir, S. Hormozi and X. Chateau, *J. Rheol.*, 2015, **59**, 1449–1486.
- 54 G. Ovarlez, S. Rodts, A. Ragouilliaux, P. Coussot, J. Goyon and A. Colin, *Phys. Rev. E: Stat., Nonlinear, Soft Matter Phys.*, 2008, **78**, 1–13.
- 55 P. Coussot, L. Tocquer, C. Lanos and G. Ovarlez, *J. Nonnewton. Fluid Mech.*, 2009, **158**, 85–90.
- 56 K. G. Hollingsworth and M. L. Johns, *J. Rheol.*, 2004, **48**, 787.
- 57 A. B. D. Brown and A. R. Rennie, *Phys. Rev. E: Stat. Phys., Plasmas, Fluids, Relat. Interdiscip. Top.*, 2000, **62**, 851–862.